Nanoscale

ROYAL SOCIETY OF CHEMISTRY

PAPER

View Article Online
View Journal

Check for updates

Cite this: DOI: 10.1039/d6nr00804f

Overcoming the bottleneck of d-band holes in plasmonic photocatalysis through molecular electronic coupling

Reha Panigrahi, Sohini Khan, Prashant Sharma, Sakshi Kuber, Gayatri Joshi, Anirban Mondal * and Saumyakanti Khatua *

Received 26th February 2026,
Accepted 5th May 2026

DOI: 10.1039/d6nr00804f

rsc.li/nanoscale

Interband excitation of plasmonic metals generates highly oxidizing d-band holes that, in principle, can drive demanding oxidative transformations. However, their ultrafast relaxation and recombination severely limit their chemical utilization. Here we identify d-band hole extraction as the intrinsic rate-limiting step in interband plasmonic photocatalysis and demonstrate that subtle modulation of metal–ligand electronic coupling provides a quantitative handle to overcome this bottleneck. Using gold nanorods functionalized with electronically distinct yet structurally analogous thiophenol ligands, we combine single-particle spectroscopy, ensemble photocatalysis, and density functional theory to establish a direct correlation between ligand HOMO–metal d-band coupling strength and overall photocatalytic efficiency. Despite comparable morphology and surface coverage, small enhancements in hole-transfer coupling accelerate oxidative charge extraction, suppress recombination, and amplify both reduction and oxidation reaction pathways. Marcus–Hush analysis reveals that hole transport is intrinsically slower than electron transfer by two orders of magnitude, rendering d-band hole extraction the dominant kinetic constraint under interband excitation. These findings establish molecular electronic coupling as a predictive descriptor for controlling d-hole flow and provide a general design principle for exploiting short-lived oxidative equivalents in plasmon-driven chemistry.

Introduction

Plasmonic metal nanostructures serve as versatile platforms for photochemical energy conversion, converting incident photons into highly energetic charge carriers capable of driving thermodynamically uphill redox processes.[1–8] The efficacy of these hot electrons and holes in interfacial catalysis is governed by their excess energy, temporal evolution, and spatial localization within the nanostructure.[9] These characteristics are inherently nanoscale in origin, arising from localized surface plasmon resonance (LSPR)-driven near-field confinement, size and shape factors, crystallographic structures, and non-equilibrium carrier generation. Under interband excitation of gold nanoparticles, d-band electrons are promoted to the sp-band, generating highly oxidizing d-band holes that are distributed across the metal volume alongside warm electrons above the Fermi level.[10] These holes exhibit sub-picosecond lifetimes (≤100 fs), short mean free path, and are generated over the entire volume of the metal, rendering their diffusive transport to surface-active sites kinetically prohibitive and subject to dominant ultrafast energy relaxation and recombination with electrons, a process that dissipates oxidative equivalent energies as heat while concomitantly curtailing electron availability for reductive half-reactions.[11] Devising strategies to selectively extract and redirect these highly energetic yet short-lived d-band holes constitutes a foundational challenge in many plasmonic photocatalysis reactions.[12] This limitation is particularly crucial for many important plasmonic-driven reactions, such as CO_2 reduction, nitrogen fixation, and solar-to-fuel conversion, where efficient oxidative half-reactions are essential for sustaining overall catalytic cycles. In such systems, the accumulation and utilization of photogenerated electrons strongly depend on the simultaneous removal of holes to maintain charge balance and suppress rapid recombination. Inefficient extraction of d-band holes therefore not only limits oxidative chemistry but also indirectly restricts electron-driven reduction pathways, ultimately reducing overall catalytic efficiency. Consequently, strategies that enable selective and efficient hot-hole extraction are expected to play a central role in the development of high-performance plasmonic photocatalysts for solar energy conversion and artificial photosynthesis.

Plasmonic antenna–reactor hybrids provide an effective strategy that promotes hot-carrier separation and transfer.[13–16] In these architectures, a plasmonic "antenna" concentrates the

---

Department of Chemistry, Indian Institute of Technology Gandhinagar, Palaj, Gujarat, 382355, India. E-mail: amondal@iitgn.ac.in, khatuask@iitgn.ac.in

electromagnetic field and generates energetic charge carriers, one of which is subsequently transferred to a catalytically active "reactor" domain where redox reactions occur. Such systems typically comprise metal–semiconductor[17–20] or metal–metal hybrids.[21–24] Although a few reports exist on specific design of antenna reactors for selective separation and transport of hot holes,[18,25–31] a vast majority of reported designs have focused predominantly on the effective harvesting and utilization of hot electrons,[32–34] leaving d-band hot holes underutilized. Alternatively, sacrificial electron donors or hole scavengers can promote charge-carrier-driven photochemistry by selectively quenching one carrier type at the interface, thereby extending the lifetime of the complementary species and suppressing recombination;[35] this approach, while effective, introduces additional chemical waste and adds to overall process costs. Recently, organic ligands have emerged as versatile mediators for charge separation in plasmonic systems, enabling directed transfer of hot carriers across metal–ligand interfaces to suppress recombination and enhance photocatalytic efficiency. In this context, the metal–ligand interface represents a critical nanoscale junction where electronic coupling can actively regulate charge-carrier extraction rather than merely serving as a passive surface modifier. In gold nanoparticles under interband excitation, polyvinylpyrrolidone (PVP) molecules have been shown to facilitate d-band hot-hole extraction.[36] Recent studies, including our prior work, demonstrated qualitative trends where aromatic thiols influence hot-carrier flow.[37,38] However, these investigations have either lacked a controlled ligand comparison that decouples electronic effects from structural variations or a direct correlation of ligand-controlled hole extraction to simultaneous oxidative and reductive reaction halves.

This study used gold nanorods capped with structurally analogous yet electronically distinct thiophenol ligands, 4-fluorothiophenol (FTP) and 4-bromothiophenol (BrTP) (hereafter referred to as Au–FTP and Au–BrTP, respectively) as a platform to dissect d-band hot-hole extraction under 488 nm interband excitation. Single-particle optical microscopy and spectroscopy, complemented by bulk photocatalysis experiments, enabled comprehensive probing of both hot-electron- and hot-hole-driven processes, establishing a complete mechanistic picture that directly relates efficient d-hole extraction to simultaneous enhancement of reduction and oxidation processes. We establish that the nanorod-bound FTP molecules enable better d-hole extraction than their BrTP counterpart producing substantially higher Au^{3+} photoreduction rates and enhanced hydroxyl radical ($^{\bullet}OH$) generation from water oxidation. First-principle theoretical analysis reveals that the favorable energetic alignment between the gold d-band and the highest occupied molecular orbital (HOMO) of FTP promotes more efficient hot-hole transfer to the ligand. This process effectively stabilizes spatially separated charge carriers, suppresses recombination, and leaves hot electrons available to drive reduction reactions. These findings demonstrate that interfacial electronic coupling serves as a tunable nanoscale design parameter that governs charge-carrier dynamics and photocatalytic efficiency. Our calculations further indicate that d-hole transfer rates are significantly slower than electron transfer, creating a photocatalytic bottleneck that underscores the need for the development of d-hole extraction strategies. By establishing a direct link between molecular-level interface design and hot-carrier utilization, this work provides generalizable design principles for overcoming kinetic limitations in plasmon-driven catalysis and for advancing nanoscale photocatalytic systems toward energy-relevant applications.

Results and discussion

The AuNRs were synthesized *via* a slightly modified seed-mediated growth method reported previously.[39,40] The extinction spectrum of the as-synthesized nanorods in aqueous medium exhibited distinct transverse (TSPR) and longitudinal (LSPR) plasmon bands centered at 530 and 650 nm, respectively (Fig. S1a). Scanning electron microscopy (SEM) confirmed their rod-like morphology, with an average length of 51 ± 5 nm and width of 21 ± 3 nm, corresponding to an aspect ratio of approximately 2.4 (Fig. S1b).

Functionalization with FTP and BrTP was performed as described in the Experimental section. Upon ligand attachment, the extinction spectra exhibited redshifts of ∼8 nm and ∼10 nm for Au–FTP and Au–BrTP, respectively (Fig. 1a), indicating modifications in the local dielectric environment that influence the plasmon resonance. Surface-enhanced Raman spectroscopy (SERS) further verified thiol binding through characteristic vibrational modes of the ligands (Fig. 1b). Prominent peaks at ∼1570 cm^{-1} (νC=C), 1070–1075 cm^{-1} (νC–S), and 1080 cm^{-1} (νC–Br) confirmed functionalization, while the absence of the 915 cm^{-1} feature excluded nonspecific adsorption of unbound thiols.[41,42] Inductively coupled plasma optical emission spectroscopy (ICP-OES) quantified thiol loading, yielding Au and S contents of 104 ± 2.5 μg and 15.47 ± 0.2 μg for Au–FTP and 112 ± 2 μg and 16 ± 2 μg for Au–BrTP (Fig. S2). The resulting Au : S ratios, 6.74 (Au–FTP) and 6.88 (Au–BrTP), indicate comparable ligand coverage in both systems. STEM–EDX elemental mapping revealed homogeneous distribution of sulfur element on the Au–FTP (Fig. 1c–f) and Au–BrTP surface (Fig. 1g–j). SEM analysis after ligand exchange confirmed that the nanorods retained their morphology and size, with average dimensions of 52 ± 4 nm (length) and 21 ± 3 nm (width) for Au–FTP (Fig. 1k), and 51 ± 3 nm (length) and 20 ± 3 nm (width) for Au–BrTP (Fig. 1l), consistent with structural stability during surface modification.

X-ray photoelectron spectroscopy (XPS) provided further insight into the surface composition (Fig. S3). For Au–FTP, the Au $4f_{7/2}$ and Au $4f_{5/2}$ peaks were located at 83.7 and 87.4 eV, respectively. The corresponding peaks for Au–BrTP appeared slightly upshifted at 83.8 and 87.5 eV. This minor shift can be attributed to the lower electronegativity of bromine compared to fluorine, resulting in altered electronic interaction with the Au surface. All observed binding energies lie within the characteristic range for metallic Au(0).

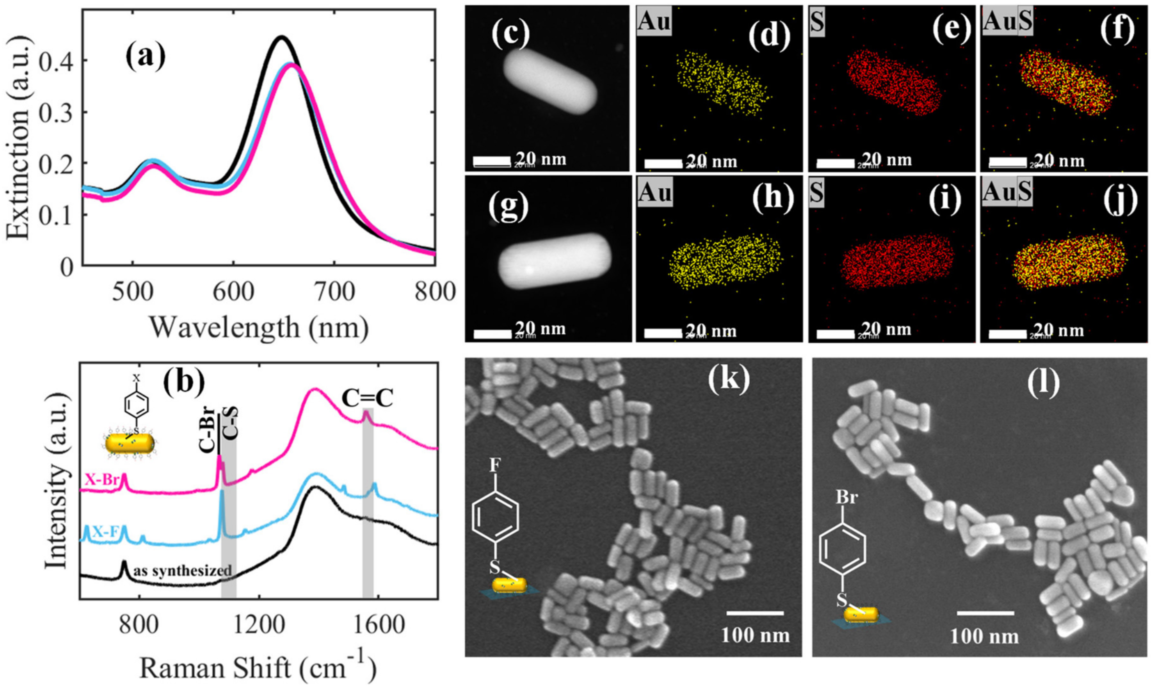

Fig. 1 Extinction spectra (a) and SERS spectra (b) of AuNR (black), Au–FTP (magenta) and Au–BrTP (blue). STEM-EDX analysis on Au–FTP (c–f) and Au–BrTP (g–j): (c and g) HAADFSTEM image, (d and h) elemental mapping images of Au, (e and i) elemental mapping images of S. (f and j) Overlay of elemental mapping of Au and S. SEM images of Au–FTP (k) and Au–BrTP (l).

To investigate ligand-dependent charge separation and photocatalytic activity, single-particle dark-field scattering (DFS) spectroscopy was employed to monitor *in situ* volume changes associated with plasmon-induced reduction of Au^{3+} to Au^0 on individual nanorods. This reduction-driven overgrowth was identified *via* LSPR spectral shifts and intensity enhancements in single-particle scattering signals. Unlike ensemble-averaged measurements, single-particle analysis directly correlates spectral evolution with individual nanorod reactivity. Control experiments showed that neither Au–FTP nor Au–BrTP nanorods exhibited any discernible spectral shift or intensity change when incubated in $HAuCl_4$ solution in the absence of illumination, confirming that no spontaneous reduction occurred in the dark (Fig. S6).

When Au–FTP nanorods immersed in $HAuCl_4$ solution were irradiated with a 488 nm laser (interband excitation) for 60 minutes, their LSPR exhibited a redshift of ~40 nm and the scattering intensity increased by approximately 2-fold. Spectral evolution of a representative nanorod is shown in Fig. 2a. The redshift suggests elongation or anisotropic overgrowth along the longitudinal axis, while the intensity enhancement reflects an increase in nanorod volume. In contrast, illumination at 633 nm (intraband excitation) did not induce any significant spectral changes (a representative nanorod is shown in Fig. 2b), indicating negligible reactivity under these conditions.

Time-dependent comparisons of plasmon shifts and intensity variations under dark, interband, and intraband conditions (Fig. 2c and d) corroborate these observations.

In comparison, Au–BrTP nanorods displayed minimal LSPR shifts (~20 nm) and no appreciable changes in scattering intensity upon interband illumination for 60 minutes (a representative nanorod is shown in Fig. 2e), suggesting a significantly slower reduction of Au^{3+} to Au^0. Intraband illumination likewise produced no notable spectral variations (a representative nanorod is shown in Fig. 2f). Comparative plasmon shifts and intensity variations under dark, interband, and intraband conditions are represented in Fig. 2g and h. Statistical analyses of 20 individual nanorods (repeated three times for reproducibility) revealed that the average scattering intensity for Au–FTP increased almost linearly with time, reaching ~2.4-fold enhancement and a simultaneous ~41 nm redshift in 60 minutes (Fig. 3a and c). These results indicate preferential tip overgrowth consistent with anisotropic Au deposition.

In contrast, Au–BrTP exhibited only a ~10% increase in intensity in 60 min resulting in a modest initial redshift (~15 nm) within 30 minutes, followed by stabilization, possibly reflecting slight side dissolution rather than overgrowth (Fig. 3b and d). Under intraband excitation, neither system showed overgrowth, confirming that photoreduction does not proceed under these conditions. A minor decrease in scattering intensity, likely due to Cl^--induced dissolution, was observed for both samples.[43]

We considered the influence of excitation polarization on photocatalytic activity, given the anisotropic geometry of gold nanorods. For this, we simulated the absorption spectrum (Fig. S7) of a 20 × 50 nm nanorod using COMSOL Multiphysics software. The absorption cross-section at 490 nm is found to

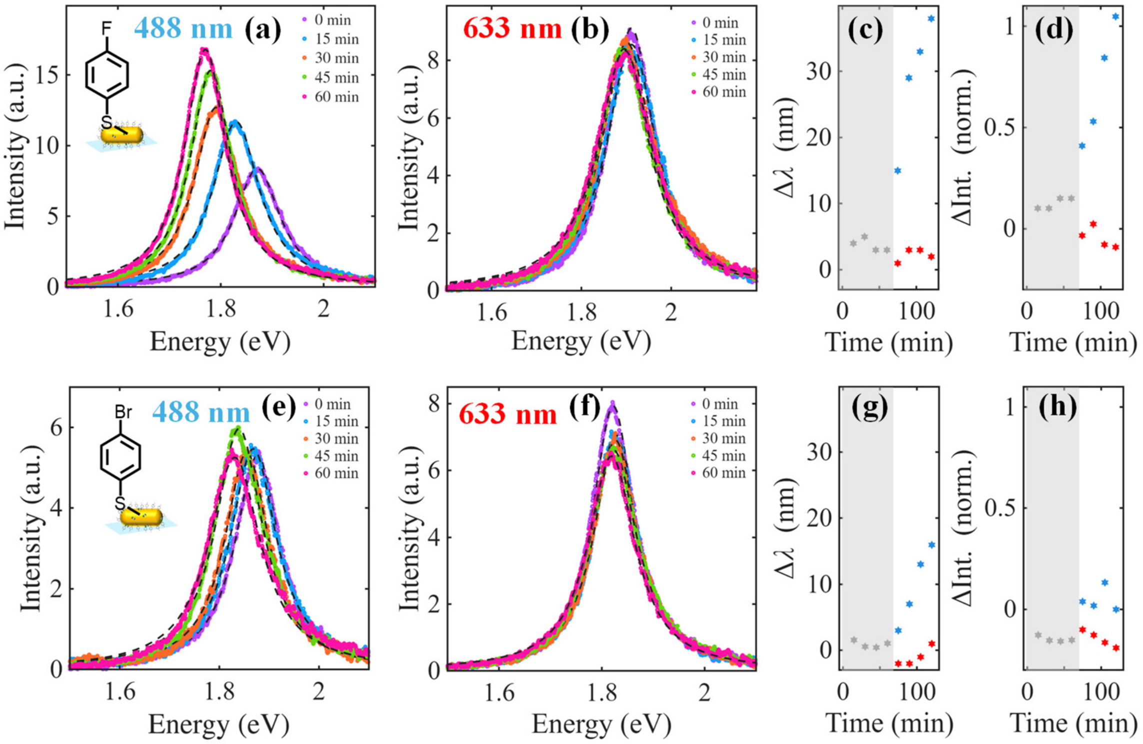

Fig. 2 Representative *in situ* spectral evolution of a single Au–FTP submerged in 20 μM $HAuCl_4$ under (a) 488 nm and (b) 633 nm illumination (c) and (d) shows the corresponding changes in LSPR and intensity, respectively, with grey markers indicating changes in dark, blue markers indicating changes under 488 nm illumination and red markers under 633 nm illumination. (e) and (f) Display the *in situ* spectral evolution of a single Au–BrTP under 488 nm and 633 nm illumination, respectively, while (g) and (h) show the corresponding changes in LSPR and intensity, respectively.

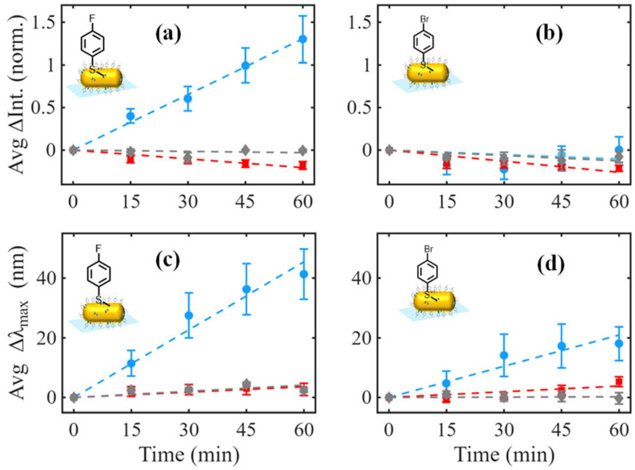

Fig. 3 Average intensity change (normalized) and LSPR shift (nm) for gold nanorods: (a and c) Au–FTP, and (b and d) Au–BrTP, under illumination with 488 nm (blue dots), 633 nm (red dots), and in the dark (grey dots).

be nearly independent of the polarization and therefore we do not expect to see any significant reactivity differences as function of the polarization for interband excitations. Under 633 nm excitation, the absorption cross-section of gold nanorods depends strongly on their orientation relative to the polarization direction, with maximum absorption when aligned parallel to the incident polarization, leading to increased photon absorption and higher charge-carrier generation. However, the energies of these carriers are determined solely by the excitation wavelength, and since the overall reactivity is limited by their insufficient energy, variations in absorption efficiency are not expected to significantly affect the reaction outcome. To further assess the role of polarization, Au^{3+} reduction experiments were performed under circularly polarized illumination at 633 nm using Au–FTP, and no significant differences in growth behavior were observed compared to linearly polarized excitation (Fig. S8). These results confirm that while carrier density depends on polarization, the overall reactivity is governed primarily by the photon energy.

SEM imaging corroborated the single-particle DFS findings. Although identical nanorods could not be imaged before and after illumination, statistical comparisons revealed distinct morphological trends. SEM images of Au–FTP nanorods post-488 nm irradiation exhibited increased average length and width (83 nm and 33 nm) relative to their initial dimensions (~55 nm and ~27 nm), consistent with photoinduced Au^{3+} reduction and Au^0 deposition (Fig. 4a, inset). Conversely, Au–BrTP nanorods retained their original size and morphology after illumination (Fig. 4b, inset), confirming negligible photoreduction.

Plasmon-induced Au^{3+} reduction is well-documented to proceed *via* hot-electron transfer.[44] To verify hot-electron involvement, Au–BrTP nanorods were irradiated under interband

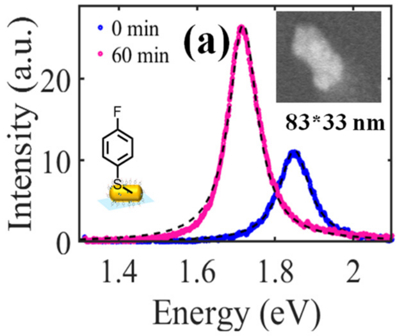

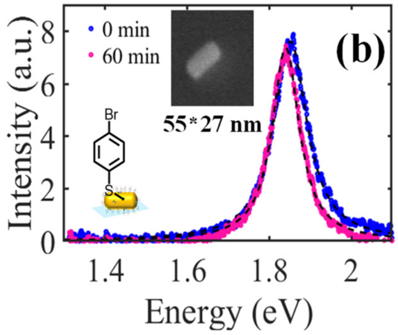

Fig. 4 (a) Dark-field (DF) scattering spectra of Au–FTP before (blue) and after (magenta) incubation in $HAuCl_4$ under 488 nm excitation for 60 min; inset: SEM image of Au–FTP after Au^0 deposition. (b) DF scattering spectra of Au–BrTP before (blue) and after (red) incubation under identical conditions; inset: SEM image of Au–BrTP after Au^0 deposition.

excitation in the presence of a hole quencher (ethanol). The addition of ethanol drastically increased the reaction rate, leading to a ~2.4-fold intensity enhancement and a ~23 ± 5 nm redshift in LSPR within 60 minutes (Fig. 5).

This enhancement indicates that photogenerated hot electrons facilitate the reduction process, while hole quenching by ethanol suppresses charge recombination. No changes were observed in the absence of illumination (Fig. S9), confirming a purely photochemical reaction pathway.

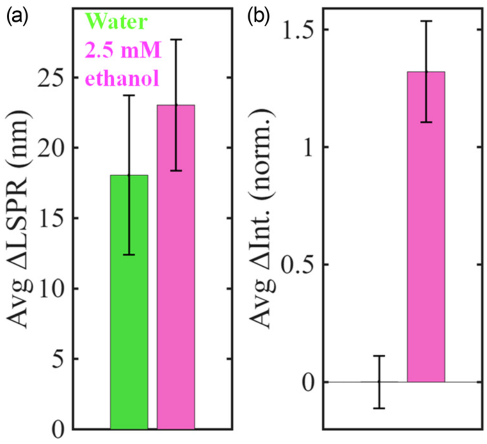

Fig. 5 Statistics of the change in (a) LSPR and (b) scattering intensity of Au–BrTP upon Au^{3+} reduction to Au^0 and subsequent deposition, from their corresponding scattering spectra, obtained in the absence of ethanol (green) and in the presence of ethanol (magenta) under 488 nm illumination.

We note that, although in the present study LSPR excitation does not significantly enhance the catalytic process, numerous reports have demonstrated that plasmon excitation can substantially promote chemical reactions. Such enhancements may arise from hot-electron transfer, electromagnetic near-field amplification, or photothermal effects, depending on the system energetics. A notable example[45] is the light-driven synthesis of shape-controlled silver nanoparticles under LED irradiation, where morphological evolution occurs in a closed system without continuous precursor supply and is governed primarily by plasmon-induced field enhancement, leading to aggregation and reshaping of pre-formed nanoparticles. In contrast, our system operates in the presence of Au^{3+} ions, enabling a continuous photochemical reduction pathway. Under these conditions, plasmonic excitation does not play a dominant role in the observed reactivity, as the hot electrons generated *via* intraband transitions lack sufficient energy to effectively drive the reduction process.

We also examined the potential contribution of photothermal effects to the observed reactivity. The estimated local temperature increase is ~71 μK at 488 nm and ~460 μK at 633 nm (detailed calculation in the SI). Such minimal temperature rises are unlikely to produce any appreciable enhancement in the reaction kinetics, indicating that photothermal contributions are negligible under the present conditions.

To rationalize the pronounced difference in reactivity between Au–FTP and Au–BrTP, we consider possible ligand-mediated mechanisms. Previous studies suggest that ligands can modulate catalytic activity by altering the interfacial electrostatic potential, thereby influencing reactant access to the surface.[46,47] However, both Au–FTP and Au–BrTP exhibited similar zeta potentials (30.9 and 38.9 mV), ruling out significant difference in electrostatic environment around the nanorods. Alternatively, the ligands may influence hot-carrier dynamics by facilitating charge separation—either by scavenging hot holes (through HOMO-level interactions) or accepting hot electrons (*via* LUMO coupling). To probe these possibilities, extensive density functional theory (DFT) calculations were performed under 488 nm excitation to evaluate charge transfer efficiencies and electronic coupling for both systems.

Fig. 6 summarizes the computed electronic structure of the Au–BrTP and Au–FTP systems. The molecular orbitals of the thiol ligands are shown in cyan, while the electronic states of the Au nanorods are shown in golden; the HOMO and LUMO levels are highlighted in blue. Under interband excitation at 488 nm (Fig. 6a and b), electronic transitions predominantly involve excitation of electrons from deeper-lying Au d-band states to sp-band states above the Fermi level, thereby generating d-band hot holes and low-energy hot electrons. To quantitatively assess the fate of these charge carriers, we evaluated the rates of charge transfer from Au d-band hole states to ligand HOMO orbitals, as well as from sp-band electrons above the Fermi level to ligand LUMO orbitals, using the Marcus–Hush formalism.

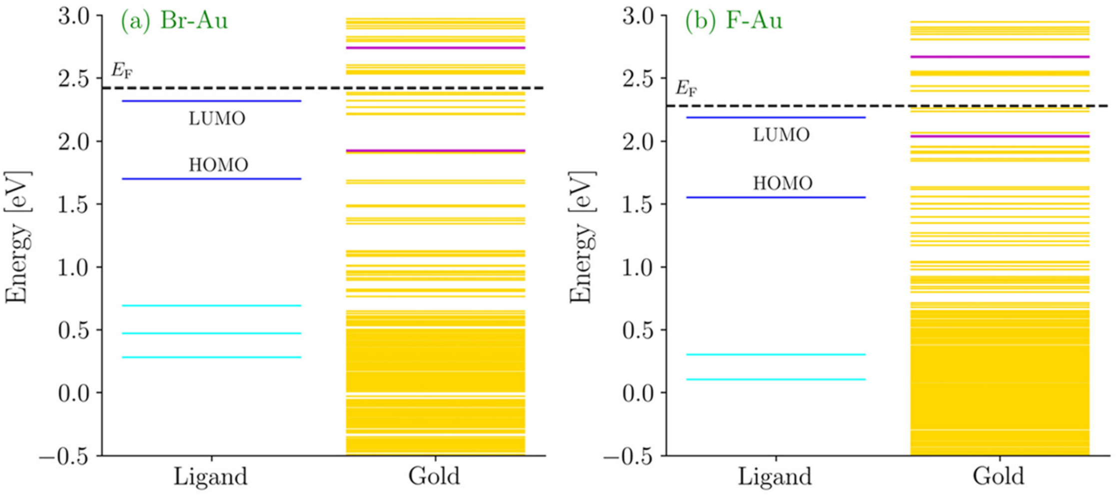

Fig. 6 Density of states and energy level plots for thiol-Au interfaces with (a) Au–BrTP and (b) Au–FTP. Golden lines represent the energy states of Au, with the upper magenta line indicating the conduction band minimum (CBM) and the lower magenta line marking the valence band maximum (VBM). The upper blue line corresponds to the LUMO and the lower green line to the HOMO of the thiol ligand. The black dotted line denotes the Fermi level of the interface.

The charge-transfer rate constant is given by

$$k = \int \frac{J^2}{\hbar}\sqrt{\frac{\pi}{\lambda kt}}\, n \exp\left(\frac{-(\lambda - \Delta E + q\eta)^2}{4\lambda kT}\right)$$

where J is the electronic coupling between a given Au state (with degeneracy n) and the relevant ligand orbital, ΔE is the energy difference between the donor and acceptor states, λ is the reorganization energy of the ligand, and η is the interfacial overpotential, taken to be zero for all calculations. Importantly, this formulation highlights that a single energy-level alignment does not govern the overall charge-transfer rate; rather, it arises from the collective contribution of coupling across all energetically accessible metal states.

Fig. 7a and b compares the coupling strength between the ligand HOMO and Au states lying below the maximum valence band, where d-band holes reside. Although the absolute differences in coupling values between Au–BrTP and Au–FTP are subtle and not immediately apparent by visual inspection, a statistically meaningful trend emerges: the F-substituted system exhibits a consistently higher probability of stronger coupling, reflected in its lower $\log J$ (*i.e.*, higher J) distribution. This enhanced coupling indicates more effective electronic communication between the ligand HOMO and the Au d-band hole states in Au–FTP. Crucially, this observation underscores that small but systematic differences in coupling strength, when integrated over the dense manifold of metal states, can translate into substantial differences in charge-transfer kinetics.

While coupling strength and energy-level alignment alone do not allow a definitive prediction of photocatalytic performance, the Marcus–Hush formalism enables a comprehensive evaluation by summing over contributions from all relevant states. The calculated rate constants reveal that, in both systems, hole transfer is intrinsically slower than electron transfer by approximately two orders of magnitude (Table 1).

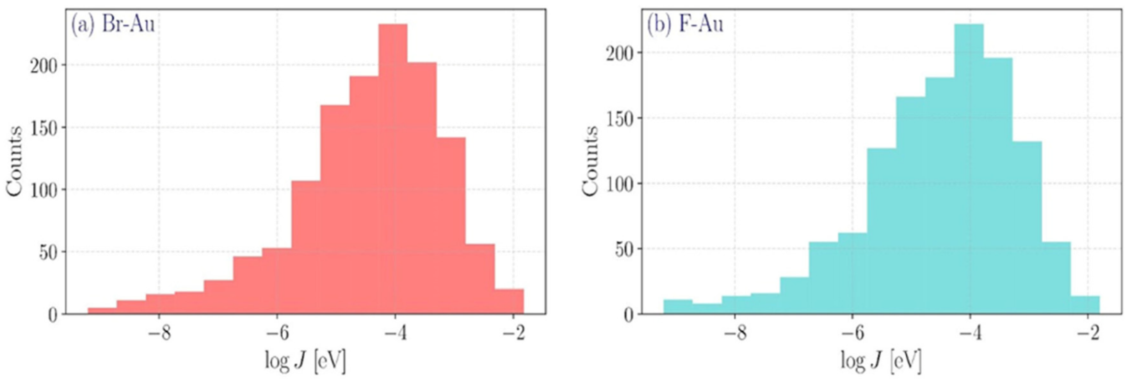

Fig. 7 Histogram showing distribution of coupling values (log J) for the two system (a) Br substituted thiol functionalized Au and (b) F substituted thiol functionalized Au.

Table 1 Calculated rates of Au d-band-to-HOMO hole transport and sp-band-to-LUMO electron transport in the Au–ligand systems

Sample	Calculated hole transport rate (s^{-1}): Au d-band to ligand HOMO	Calculated electron transport rate (s^{-1}): Au sp-band to ligand LUMO
4-FTP	2.81×10^6	2.51×10^8
4-BrTP	1.88×10^6	1.82×10^9

This significant disparity establishes d-band hole extraction as the rate-limiting step in the overall photocatalytic process under interband excitation.[48] Notably, although Au–BrTP exhibits an electron transfer rate that is nearly an order of magnitude higher than that of Au–FTP, its overall photocatalytic activity is significantly lower. This apparent contradiction is resolved by considering the hole-transfer kinetics: Au–BrTP suffers from markedly slower hole extraction due to weaker coupling between the ligand HOMO and the Au d-band states, leading to rapid recombination of holes with conduction-band electrons. In contrast, Au–FTP exhibits a faster hole transfer rate, enabled by stronger HOMO–d-band coupling. This efficient hole extraction stabilizes spatially separated charge carriers, suppresses recombination, and prolongs the lifetime of hot electrons in the sp-band.[49] As a result, these electrons can participate more effectively in plasmon-induced reduction reactions, such as the conversion of Au^{3+} to Au^0.

Overall, these results establish that even modest enhancements in electronic coupling between ligand HOMO levels and Au d-band states can decisively control photocatalytic efficiency when hole transfer is rate-limiting. The findings highlight ligand-mediated modulation of coupling—not merely energetic alignment—as a critical design parameter for exploiting d-band hot holes in interband-driven plasmonic photocatalysis.

It is important to note that the present theoretical framework is specifically focused on the interfacial transfer of photogenerated charge carriers from the metal to the ligand and does not explicitly incorporate the preceding processes of carrier generation, transport within the metal, or plasmonic near-field enhancement. These processes are inherently nanoscale in nature and are strongly governed by nanoparticle geometry, size, and optical response.[50,51] In anisotropic gold nanorods, for example, aspect-ratio-dependent plasmonic modes give rise to localized electromagnetic field enhancement and spatially heterogeneous excitation profiles, which can significantly influence both the generation rate and spatial distribution of hot carriers.[52] Furthermore, because the dimensions of the nanostructure are comparable to carrier mean free paths, the high surface-to-volume ratio increases the probability that photogenerated carriers reach the interface prior to relaxation, thereby enhancing the efficiency of interfacial extraction processes. Thus, the overall photocatalytic performance is determined by the combined influence of charge-carrier generation and extraction dynamics. In the present study, however, we specifically investigated the ligand-assisted d-band hole extraction process with the assumption that the intrinsic plasmonic charge-carrier generation characteristics of the gold nanorods remain largely unaffected by the ligand environment.

To further substantiate that charge separation is more efficient in Au–FTP, we examined the participation of hot holes by monitoring the water oxidation reaction. Previous studies have shown that plasmon-generated hot holes can drive water oxidation, leading to the formation of $^{\bullet}$OH.[53] Because the amount of $^{\bullet}$OH formed at the single-particle level is exceedingly small and difficult to detect spectroscopically, we performed ensemble measurements using a densely packed film of functionalized nanorods prepared by drop-casting a concentrated colloidal solution onto a glass substrate (Fig. S12). The substrate was immersed in water and illuminated with a 440 nm light-emitting diode (LED). The generation of $^{\bullet}$OH was monitored using terephthalic acid (TPA) as a fluorescent probe, which reacts with $^{\bullet}$OH to form 2-hydroxyterephthalic acid (HTPA), exhibiting strong fluorescence around 430 nm (Fig. 8a). Fig. 8b (inset) presents the fluorescence spectra recorded after 5 hours of illumination for both Au–FTP and Au–BrTP samples. The emission intensity corresponding to HTPA formation was significantly higher for Au–FTP, indicating a greater yield of hydroxyl radicals compared to Au–BrTP. Quantitative analysis of the fluorescence data revealed that Au–FTP nanorods generated approximately twice the amount of $^{\bullet}$OH (347 μM mg^{-1} Au) relative to Au–BrTP (177 μM mg^{-1} Au) under identical conditions. These findings are consistent with our theoretical results, which predict faster hole transfer kinetics in Au–FTP. Importantly, no $^{\bullet}$OH generation

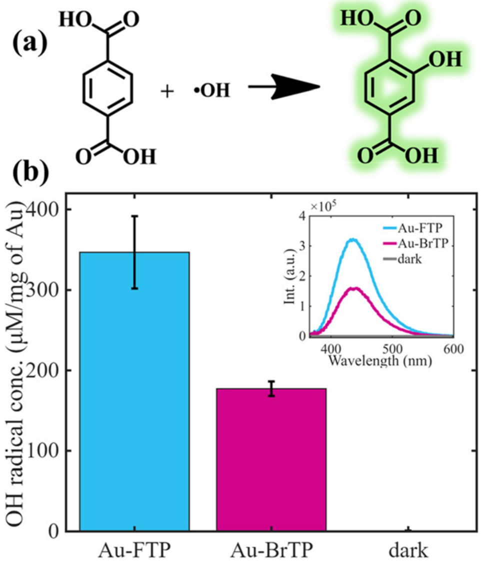

Fig. 8 (a) A reaction scheme for the detection of $^{\bullet}$OH detection using terephthalic acid. (b) OH radical generation via water oxidation using Au–FTP (blue) and Au–BrTP (magenta) as catalysts, under 440 LED illumination, and in the dark. The inset shows the fluorescent peak (at 430 nm) generated due to HTPA formed after the generation of the OH radical from water oxidation.

was observed in the absence of light excitation or without the nanorods, confirming the photocatalytic origin of the reaction.

Fig. 9 presents a schematic illustration summarizing the proposed mechanism of ligand-mediated charge separation and photocatalytic behavior in the functionalized Au nanorods. Under intraband excitation at 633 nm, excitation of conduction band (sp-band) electrons generates hot electrons above Fermi Level and warm hole near the Fermi level. Although these hot electrons can transiently possess sufficient kinetic energy, their lifetime is extremely short due to rapid electron–electron scattering and recombination with low-energy holes that remain localized within the metal. In both Au–FTP and Au–BrTP, most of these holes have energies below the ligand HOMO level, hindering their transfer across the metal–ligand interface. This inefficient hole extraction leads to a fast recombination of photogenerated carriers, forming a bottleneck that prevents the reduction of Au^{3+} at the nanoparticle surface.

In contrast, interband excitation (λ = 488 nm) directly excites electrons from the d-band to the sp-band of Au, generating deep d-band holes characterized by higher potential energy. These hot holes can be efficiently transferred to the HOMO of the surface-bound thiol ligands, a process that is energetically more favorable for the Au–FTP compared to Au–BrTP. The efficient hole transfer to the ligand stabilizes charge separation by spatially isolating the photogenerated electrons, thereby enhancing their lifetime and reducing the rate of electron–hole recombination. The hot electrons in the sp-band subsequently drive the reduction of Au^{3+} ions in the surrounding medium to Au^0, promoting anisotropic overgrowth along the nanorod tips. Although the bulkier BrTP ligand could, in principle, introduce additional steric constraints that affect interfacial accessibility of Au^{3+} ions, control experiments performed in the presence of a hole scavenger revealed a substantial enhancement in the photoreduction rate (Fig. 5), similar to that observed for FTP-functionalized nanorods. These observations indicate that the overall reaction kinetics are governed predominantly by the efficiency of d-band hole extraction and charge separation rather than by steric limitations associated with ligand structure. This ligand-facilitated hole extraction thus plays a critical role in enabling the hot-electron–driven photoreduction reaction and explains the markedly higher photocatalytic efficiency observed for Au–FTP relative to Au–BrTP under interband excitation.

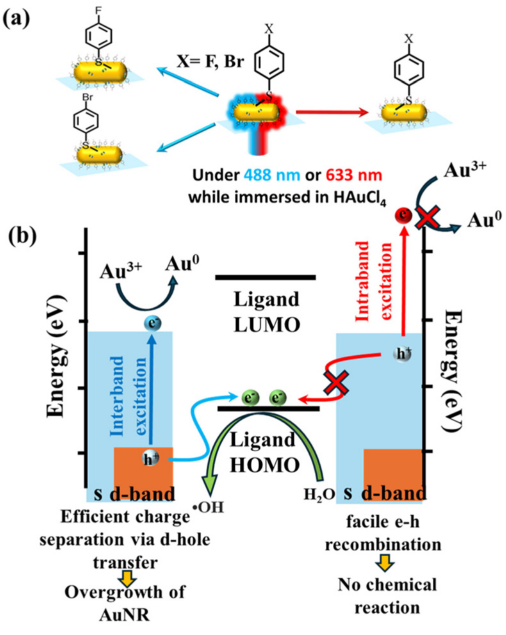

Fig. 9 Light driven Au^{3+} reduction as model reaction (a) schematic of volume change when Au–FTP and Au–BrTP immersed in $HAuCl_4$ are irradiated with 488 nm (blue) and 633 nm (red) lasers. (b) Schematic energy diagram illustrating the mechanism of effective d-hole transport for interband excitation, which promotes efficient charge separation and subsequent overgrowth of AuNRs, whereas rapid electron–hole recombination for intraband excitation does not lead to any chemical reaction.

We note that in principle, the crystallographically distinct tip and side facets of nanorods may differ in their local density of electronic states, surface coordination environment, and ligand adsorption characteristics, which could influence local interfacial charge-transfer kinetics. In our experiments, however, we did not observe evidence for substantial differences in ligand binding affinity or surface functionalization density between the tips and side facets for either 4-FTP or 4-BrTP ligands (Fig. 1e and i). Accordingly, our current experimental and theoretical analyses treat the ligand layer as approximately uniform across the nanorod surface. Nevertheless, the spatial distribution of hot carriers in anisotropic plasmonic nanostructures is an important nanoscale consideration. Studies have shown hot electron localization coincides with electric near-field distribution leading to localized chemistry at tips of the gold nanorods[54] or nanoprisms.[55] In a recent study, Link and co-workers,[56] have shown that d-band holes generated under optical excitation can exhibit preferential localization near nanorod tips due to geometry-dependent plasmonic and electronic effects. Such localization could potentially enhance the probability of interfacial hole transfer at these regions even in the absence of strong facet-dependent ligand adsorption differences. We therefore expect that the overall hole-extraction process likely reflects an interplay between nanoscale carrier localization and interfacial electronic coupling.

Conclusion

In conclusion, this study identifies the ligand electronic structure as a critical design parameter for modulating interfacial hot-carrier dynamics in plasmonic metals, particularly for harnessing the often-overlooked contribution of hot holes. By integrating experiments and theory, we establish a clear mechanistic framework demonstrating how small-molecule thiol ligands can effectively extract d-band holes, thereby promote charge separation and enhance photocatalytic efficiency under interband excitation.

These ligand-directed design principles provide a general strategy for tailoring hot-carrier pathways and are expected to contribute to the development of next-generation plasmonic photocatalysts for a broad range of photoelectrochemical and energy conversion applications.

Experimental methods

Synthesis of gold nanorods used for experiments

Materials. Chloroauric acid trihydrate ($HAuCl_4$, 99.9%, 520918-1G, Sigma Aldrich), silver nitrate ($AgNO_3$), ascorbic acid, sodium borohydride ($NaBH_4$), cetyltrimethylammonium bromide (CTAB), purchased from Sigma-Aldrich were used as received. Millipore water with a resistivity of 18.2 MΩ cm was used for the synthesis.

Synthesis of seed solution. To synthesize the seed solution, 5 mL of 0.2 M CTAB was first taken in a vial. Next, 5 mL of 0.5 mM $HAuCl_4$ was added. The mixture was stirred for a few seconds to yield a homogeneous solution. To the above solution, 200 μL of freshly prepared 0.01 M $NaBH_4$ was added rapidly under vigorous stirring. As the reaction progressed, the solution changed from pale yellow to brownish, indicating the formation of small gold seed nanoparticles. The seed solution was left undisturbed at 30 °C for 30 minutes to age before use in the growth process.

Preparation of growth solution. To prepare the growth solution, 10 mL of 0.2 M CTAB was taken in a vial and kept in a water bath maintained at 30 °C. To this 100 μL of 4mM $AgNO_3$ was added, and the solution was kept undisturbed for 15 minutes. Further, 10 mL of 1 mM $HAuCL_4$ was added, followed by the addition of 140 μL of 78.8 mM ascorbic acid. When ascorbic acid was added, the solution became colourless. 12 μL of the seed solution was added to the prepared growth solution. This solution was kept undisturbed for 12 h for nanorods to grow. The prepared gold nanorods were centrifuged and redispersed in a 200 μM CTAB solution for storage and experimental use.

Bulk characterization of AuNR

The extinction spectrum of prepared gold nanorods was acquired in aqueous medium with a UV-vis (Analytik Jena) spectrophotometer. Further, the morphological analysis of the nanorods was done with Scanning electron microscopy (Jeol FESEM).

Surface modification and sample preparation of gold nanorods

CTAB was partially removed by centrifuging the synthesized AuNR solution at 8000 rpm for 5 min. The supernatant was carefully discarded, and the residue was redispersed in Milli-Q water to achieve a tenfold dilution. Subsequently, 20 μL of a 10 mM thiol solution in ethanol was added to the diluted AuNR dispersion, and the mixture was incubated for a few minutes. The functionalized nanorod solution was again centrifuged to remove unbound thiols. The supernatant was discarded, and the residue was redispersed in Milli-Q water. The solution was characterized using UV-vis spectroscopy, SEM and was further used for elemental mapping, Surface Enhanced Raman- Spectroscopy (SERS) and Inductively Coupled Plasma Optical Emission Spectrometry (ICP-OES) analyses.

Characterization of functionalized gold nanorods with UV-vis spectroscopy, Raman spectroscopy, and elemental mapping

The functionalized nanorods were characterized using UV-vis spectroscopy. Further SERS analyses were performed using an *in situ* Raman probe (Kaiser Raman Rxn System) equipped with a 785 nm laser diode (10 mW power, 10 s exposure time). The presence of ligands on the surface of the nanorods was also confirmed with Transmission Electron Microscope (TEM) and Scanning Transmission Electron Microscope (STEM) mapping using a Thermo Titan Themis, 300 kV, equipped with a CCD camera for image acquisition. TEM samples were prepared by drop-casting 5 μL of the functionalized AuNR solution onto a carbon-coated 300-mesh copper grid. The presence of tiols on the functionalized AuNRs was confirmed from elemental mapping by mapping –S elements (Fig. S2).

Sample preparation for ICP-OES analysis

The functionalized nanorods were deposited by drop-casting the solution onto cleaned glass slides and allowing them to dry. The glass slides were then digested in aqua regia for 6 hours. The digested samples were subsequently diluted in a 2% HNO_3 solution and used for ICP-OES analysis.

Sample preparation for single particle experiments

Corning cover glasses (24 × 60 mm and 24 × 40 mm) were cleaned by sequential sonication in methanol (15 min), acetone (15 min), and isopropyl alcohol (15 min). The cover glasses were dried under a nitrogen stream and subjected to ozone cleaning for 30 min. A 10 μL of thiolated AuNR solution was spin-coated onto the cleaned cover glasses. The substrate was then washed with water and ethanol to remove unbound thiols from the glass surface, followed by drying under a stream of nitrogen.

Preparation of flowcell

The flow cell was constructed using an aluminum frame with two flow channels. A 24 × 40 mm Corning cover glass was placed at the centre of the flow cell and secured with polydimethylsiloxane (PDMS). A 2 mm thick layer of PDMS was spread onto the aluminium frame and left overnight to solidify partially. A flow channel was then cut through the semi-solid PDMS, aligning with the flow channels of the aluminum frame. Coverslips with spin-coated samples were placed on the PDMS, ensuring that the nanorod-coated surface faced the interior of the flow cell.

Single particle spectroscopy

All dark-field measurements were performed using a home-built confocal microscope consisting of an inverted microscope (Olympus IX73P2F), equipped with an XYZ nano-positioning stage (PIMars P-561.3CD), a 488 nm laser (Coherent

Obis), a 633 nm laser (Oxxius), an avalanche photodiode (APD), and a spectrometer (Andor Kymera 328i-A) integrated with a CCD camera (DU416A-LDC-DD). A 100 W halogen lamp, integrated with the microscope, was used to illuminate the nanorods with white light through a condenser (N.A. = 1.4) at an oblique angle. The scattered light from the nanorods was collected using an oil immersion objective (Olympus, 60×, N.A. = 0.65, UPlanFL N) and directed to the APD (Excelitas) and spectrometer to record both the scattering image and the corresponding spectrum of the nanorods, respectively. The movement of the piezo stage was controlled *via* a LabVIEW program, enabling the acquisition of nanorod scattering images by the APD with an integration time of 10 ms. Spectral data were obtained by directing the scattered light to the spectrometer using a flip mirror. All acquired data were analyzed using custom MATLAB scripts. The intensity of each spectrum was corrected using the formula:

$$\text{Intensity} = (\text{signal-background})/(\text{background-darkcount})$$

Correlation of darkfield and SEM image

To trace the nanorod volume changes, single-particle experiments were performed on a glass slide with a defined mark. The reaction was carried out near those mark to facilitate easy localization in SEM imaging. After the reaction, the slide was sputter-coated with platinum to ensure conductivity. The same region near the mark was then located, and SEM images of the corresponding nanorods were acquired (Fig. S11).

Generation of hydroxyl radical from water oxidation by hot holes

For the $^{\bullet}$OH experiments, the functionalized AuNRs were first dried onto cleaned glass slides. Prior to use in the water oxidation experiments, the slides were washed thoroughly with ethanol followed by water. A 0.5 mM TPA solution in water was prepared in a 15 mL vial, and the functionalized glass slides were then immersed in this solution. The vial was sealed with a septum and Parafilm, followed by Ar purging for 30 minutes. After purging, the vial was resealed and irradiated with a 440 nm LED for 5 hours. Following irradiation, the sample was examined under fluorescence to detect 2-hydroxyterephthalic acid (HTPA) formed from the reaction between $^{\bullet}$OH radicals generated during water oxidation and the TPA present in solution.

Density functional theory studies

DFT (Density Functional Theory)[57,58] simulations were carried out on a model of a gold slab having a substituted thiol attached to its surface *via* an S–Au bond. The gold slab consisting of 288 atoms was arranged in four layers, out of which the top two layers were kept mobile to represent the surface, and the bottom layers were held frozen to represent the bulk.[59] All calculations were conducted using the *Quickstep* module of the CP2K[60,61] program. The convergence criteria for nuclear forces were set to 10^{-4} a.u. DFT calculations were performed using a mixed basis set scheme designed to ensure a balance between computational efficiency and accuracy. Au atoms were described using the TZ-GTH basis set, while the TZVP-MOLOPT-GTH[62,63] basis set was employed for all other lighter elements, as it provides reliable accuracy for both molecular and condensed-phase systems. Exchange-correlation potentials were described using the generalized gradient approximation (GGA) with the Perdew–Burke–Ernzerhof (PBE) functional. The energy cutoff for the auxiliary plane wave expansion of the charge density was set to 415 Ry. Valence electrons were explicitly modeled, while core electrons were represented using Goedecker–Teter–Hutter (GTH) pseudopotentials.[64,65]

The Projection Operator Diabatization (POD) method was applied to the optimized system to find out the energy levels and coupling values of the thiol adsorbate (treated as one block) and Au slab (treated as another block). Fermi–Dirac smearing with an electronic temperature of 298.15 K was employed to maintain fractional occupation near the Fermi energy. The interfacial electronic structure characterization was performed through the PROPERTIES module of CP2K, with particular emphasis on the ET_COUPLING functionality for determination of orbital/state energy levels and electronic coupling matrix elements between the gold substrate and molecular ligands. Simulated parameters obtained from the POD calculation were incorporated into the Marcus–Hush equation:[66,67]

$$k_{\text{et}} = \frac{(2\pi)}{\hbar}\int J_{\text{E}}{}^{2}(E)\frac{1}{1+\exp\frac{(E-E_{\text{F}})}{kT}} n(E)\frac{1}{\sqrt{(4\pi\lambda kT)}}\exp\frac{-(\lambda+\Delta E+q\eta)^{2}}{4\lambda kT}\text{d}E$$

Here, J_{E} represents the coupling between the ligand's orbital (HOMO) and the Au states at energy level E, q denotes the elementary charge, with a value of 1.6×10^{-19} coulombs, and $n(E)$ represents the density of states at the energy level E, ΔE is the energy difference between E and the ligand orbital (HOMO), E_{F} is the Fermi level, λ is the reorganization energy of the adsorbed species, η is the overpotential of metal surface, k is the Boltzmann constant, and T is the temperature (298.15 K). All these parameters, when taken together, can give us an idea about the rate of charge (hole, in this case) transfer across a functionalized interface, denoted here by k_{et}. Here, $q\eta$ was considered as 0 eV and λ as 0.1 eV, and k_{et} was calculated using the energy level and coupling values of the concerned states of Au and the orbital of thiol.

Author contributions

R. P. and S. K. conceived the main idea. All single-particle experiments were done by R. P. Bulk photochemical studies were done by R. P., S. K., and G. J. Optical microscopy–SEM correlation was carried out by R. P. and P. S. Sa. K. contributed equally to this work. All data analysis was performed by R. P. The DFT calculations were performed by Sh. K. and A. M. R. P., A. M., and S. K. wrote the manuscript. All authors have given approval to the final version of the manuscript.

Conflicts of interest

The authors declare no competing financial interest.

Data availability

The supporting data has been provided as part of the supplementary information (SI). Supplementary information: ICP-OES, XPS, control experiment data analysis and further experimental details. See DOI: https://doi.org/10.1039/d6nr00804f.

Acknowledgements

We acknowledge financial support from the Science and Engineering Research Board, India (CRG/2020/003471) and the Anusandhan National Research Foundation, India (ANRF/ARG/2025/002402/CS). R. P. acknowledges the University Grants Commission (UGC) for the Savitribai Jyotirao Phule Fellowship for Single Girl Child (SJSGC) fellowship. G. J. acknowledges the support from DST WISE-PDF (DST/WISE-PDF/CS-130/2023). We also thank the Central Instrumentation facility at IIT Gandhinagar (CIF-IITGN) for FESEM facility, Prof. Sameer Dalvi for the Raman Instrument, Mr Abinash Parida and Parth Shah for TEM analysis, Arunima Thottathil and Ankita Pattanayak for ICP-OES analysis, and Pooja Hingu for XPS analysis.

References

1 Y. Sun and Z. Tang, Photocatalytic Hot-Carrier Chemistry, *MRS Bull.*, 2020, **45**(1), 20–25, DOI: 10.1557/mrs.2019.290.

2 S. Mukherjee, F. Libisch, N. Large, O. Neumann, L. V. Brown, J. Cheng, J. B. Lassiter, E. A. Carter, P. Nordlander and N. J. Halas, Hot Electrons Do the Impossible: Plasmon-Induced Dissociation of H2 on Au, *Nano Lett.*, 2013, **13**(1), 240–247, DOI: 10.1021/nl303940z.

3 L. Zhou, D. F. Swearer, C. Zhang, H. Robatjazi, H. Zhao, L. Henderson, L. Dong, P. Christopher, E. A. Carter, P. Nordlander and N. J. Halas, Quantifying Hot Carrier and Thermal Contributions in Plasmonic Photocatalysis, *Science*, 2018, **362**(6410), 69–72, DOI: 10.1126/science.aat6967.

4 R. Verma, R. Belgamwar and V. Polshettiwar, Plasmonic Photocatalysis for CO2 Conversion to Chemicals and Fuels, *ACS Mater. Lett.*, 2021, **3**(5), 574–598, DOI: 10.1021/acsmaterialslett.1c00081.

5 A. Choudhary, A. Halder, P. Aggarwal and V. Govind Rao, Plasmonic Chemistry for Sustainable Ammonia Production, *Commun. Mater.*, 2024, **5**(1), 69, DOI: 10.1038/s43246-024-00510-7.

6 R. C. Elias, B. Yan and S. Linic, Probing Spatial Energy Flow in Plasmonic Catalysts from Charge Excitation to Heating: Nonhomogeneous Energy Distribution as a Fundamental Feature of Plasmonic Chemistry, *J. Am. Chem. Soc.*, 2024, **146**(43), 29656–29663, DOI: 10.1021/jacs.4c10395.

7 R. K. Kashyap and P. P. Pillai, Plasmonic Nanoparticles Boost Solar-to-Electricity Generation at Ambient Conditions, *Nano Lett.*, 2024, **24**(18), 5585–5592, DOI: 10.1021/acs.nanolett.4c00925.

8 S.-C. Huang, X. Wang, Q.-Q. Zhao, J.-F. Zhu, C.-W. Li, Y.-H. He, S. Hu, M. M. Sartin, S. Yan and B. Ren, Probing Nanoscale Spatial Distribution of Plasmonically Excited Hot Carriers, *Nat. Commun.*, 2020, **11**(1), 4211, DOI: 10.1038/s41467-020-18016-4.

9 T. P. Rossi, P. Erhart and M. Kuisma, Hot-Carrier Generation in Plasmonic Nanoparticles: The Importance of Atomic Structure, *ACS Nano*, 2020, **14**(8), 9963–9971, DOI: 10.1021/acsnano.0c03004.

10 Q. Nguyen and A. Baldi, Size Matters: D-Band Holes Drive Plasmonic Chemistry in Gold, *Nano Lett.*, 2025, **25**(40), 14704–14709, DOI: 10.1021/acs.nanolett.5c03849.

11 S. A. Lee, C. T. Kuhs, E. K. Searles, H. O. Everitt, C. F. Landes and S. Link, D -Band Hole Dynamics in Gold Nanoparticles Measured with Time-Resolved Emission Upconversion Microscopy, *Nano Lett.*, 2023, **23**(8), 3501–3506, DOI: 10.1021/acs.nanolett.3c00622.

12 M. Ahlawat, D. Mittal and V. Govind Rao, Plasmon-Induced Hot-Hole Generation and Extraction at Nano-Heterointerfaces for Photocatalysis, *Commun. Mater.*, 2021, **2**(1), 114, DOI: 10.1038/s43246-021-00220-4.

13 D. F. Swearer, H. Zhao, L. Zhou, C. Zhang, H. Robatjazi, J. M. P. Martirez, C. M. Krauter, S. Yazdi, M. J. McClain, E. Ringe, E. A. Carter, P. Nordlander and N. J. Halas, Heterometallic Antenna–reactor Complexes for Photocatalysis, *Proc. Natl. Acad. Sci. U. S. A.*, 2016, **113**(32), 8916–8920, DOI: 10.1073/pnas.1609769113.

14 A. Dhankhar and P. P. Pillai, Plasmonic Antenna–Reactor Photocatalysts Based on Anisotropic Gold–Rhodium Superstructures for Biological Cofactor Regeneration, *Chem. Mater.*, 2024, **36**(20), 10227–10237, DOI: 10.1021/acs.chemmater.4c01966.

15 F. Tong, X. Liang, X. Bao and Z. Zheng, Photocatalysis on Hybrid Plasmonic Nanomaterials: From Catalytic Mechanism Study at Single-Particle Level to Materials Design, *ACS Catal.*, 2024, **14**(15), 11425–11446, DOI: 10.1021/acscatal.4c03566.

16 S. Linic, S. Chavez and R. Elias, Flow and Extraction of Energy and Charge Carriers in Hybrid Plasmonic Nanostructures, *Nat. Mater.*, 2021, **20**(7), 916–924, DOI: 10.1038/s41563-020-00858-4.

17 N. Kunthakudee, P. Ramakul, K. Serivalsatit and M. Hunsom, Photosynthesis of Au/TiO2 Nanoparticles for Photocatalytic Gold Recovery from Industrial Gold-Cyanide Plating Wastewater, *Sci. Rep.*, 2022, **12**(1), 21956, DOI: 10.1038/s41598-022-24290-7.

18 J. S. DuChene, G. Tagliabue, A. J. Welch, X. Li, W.-H. Cheng and H. A. Atwater, Optical Excitation of a Nanoparticle Cu/p-NiO Photocathode Improves Reaction Selectivity for CO2 Reduction in Aqueous Electrolytes, *Nano Lett.*, 2020, **20**(4), 2348–2358, DOI: 10.1021/acs.nanolett.9b04895.

19 B. Foerster, M. Hartelt, S. S. E. Collins, M. Aeschlimann, S. Link and C. Sönnichsen, Interfacial States Cause Equal

Decay of Plasmons and Hot Electrons at Gold–Metal Oxide Interfaces, *Nano Lett.*, 2020, **20**(5), 3338–3343, DOI: 10.1021/acs.nanolett.0c00223.

20 T. Yang, B. Lu, Y. Zuo and J. Huang, Configuration Engineering of Plasmonic-Metal/Semiconductor Nanohybrids for Solar Fuel Production, *Chem. Mater.*, 2025, **37**(5), 1685–1715, DOI: 10.1021/acs.chemmater.4c03170.

21 M. Herran, S. Juergensen, M. Kessens, D. Hoeing, A. Köppen, A. Sousa-Castillo, W. J. Parak, H. Lange, S. Reich, F. Schulz and E. Cortés, Plasmonic Bimetallic Two-Dimensional Supercrystals for H2 Generation, *Nat. Catal.*, 2023, **6**(12), 1205–1214, DOI: 10.1038/s41929-023-01053-9.

22 S. Sim, A. Beierle, P. Mantos, S. McCrory, R. P. Prasankumar and S. Chowdhury, Ultrafast Relaxation Dynamics in Bimetallic Plasmonic Catalysts, *Nanoscale*, 2020, **12**(18), 10284–10291, DOI: 10.1039/D0NR00831A.

23 X. Yang, Q. Wang, S. Qing, Z. Gao, X. Tong and N. Yang, Modulating Electronic Structure of an Au–Nanorod–Core–PdPt–Alloy–Shell Catalyst for Efficient Alcohol Electro–Oxidation, *Adv. Energy Mater.*, 2021, **11**(26), 2100812, DOI: 10.1002/aenm.202100812.

24 U. Aslam, S. Chavez and S. Linic, Controlling Energy Flow in Multimetallic Nanostructures for Plasmonic Catalysis, *Nat. Nanotechnol.*, 2017, **12**(10), 1000–1005, DOI: 10.1038/nnano.2017.131.

25 F. Kiani, A. R. Bowman, M. Sabzehparvar, C. O. Karaman, R. Sundararaman and G. Tagliabue, Transport and Interfacial Injection of D-Band Hot Holes Control Plasmonic Chemistry, *ACS Energy Lett.*, 2023, **8**(10), 4242–4250, DOI: 10.1021/acsenergylett.3c01505.

26 A. Al-Zubeidi, Y. Wang, J. Lin, C. Flatebo, C. F. Landes, H. Ren and S. Link, D-Band, Holes React at the Tips of Gold Nanorods, *J. Phys. Chem. Lett.*, 2023, **14**(23), 5297–5304, DOI: 10.1021/acs.jpclett.3c00997.

27 R. Kamarudheen, G. J. W. Aalbers, R. F. Hamans, L. P. J. Kamp and A. Baldi, Distinguishing Among All Possible Activation Mechanisms of a Plasmon-Driven Chemical Reaction, *ACS Energy Lett.*, 2020, **5**(8), 2605–2613, DOI: 10.1021/acsenergylett.0c00989.

28 Y. T. Wang, M.-Y. Kuo, Y. A. Chien, C. Y. Chen, T. F. M. Chang, M. Sone and Y. J. Hsu, Review of Hot-Hole Photocatalysis in Plasmonic Nanostructures, *ACS Appl. Nano Mater.*, 2026, **9**(5), 2154–2175, DOI: 10.1021/acsanm.5c05716.

29 M. Okazaki, Y. Suganami, N. Hirayama, H. Nakata, T. Oshikiri, T. Yokoi, H. Misawa and K. Maeda, Site-Selective Deposition of a Cobalt Cocatalyst onto a Plasmonic Au/TiO2 Photoanode for Improved Water Oxidation, *ACS Appl. Energy Mater.*, 2020, **3**(6), 5142–5146, DOI: 10.1021/acsaem.0c00857.

30 H. Lee, Y. Park, S. Nah, M. Kang, M. Lee and J. Y. Park, Reconfiguring Hot-Hole Flux via Polarity Modulation of p-GaN in Plasmonic Schottky Architectures, *Sci. Adv.*, 2025, **11**(10), eadu0086, DOI: 10.1126/sciadv.adu0086.

31 H. Nishi and T. Tatsuma, Mechanistic Analysis of Plasmon-Induced Charge Separation by the Use of Chemically Synthesized Gold Nanorods, *J. Phys. Chem. C*, 2018, **122**(4), 2330–2335, DOI: 10.1021/acs.jpcc.7b11528.

32 D. Lei, D. Su and S. A. Maier, New Insights into Plasmonic Hot-Electron Dynamics, *Light. Sci. Appl.*, 2024, **13**(1), 243, DOI: 10.1038/s41377-024-01594-z.

33 A. Dey, V. R. Silveira, R. B. Vadell, A. Lindblad, R. Lindblad, V. Shtender, M. Görlin and J. Sá, Exploiting Hot Electrons from a Plasmon Nanohybrid System for the Photoelectroreduction of CO2, *Commun. Chem.*, 2024, **7**(1), 59, DOI: 10.1038/s42004-024-01149-8.

34 L. Zhou, Q. Huang and Y. Xia, Plasmon-Induced Hot Electrons in Nanostructured Materials: Generation, Collection, and Application to Photochemistry, *Chem. Rev.*, 2024, **124**(14), 8597–8619, DOI: 10.1021/acs.chemrev.4c00165.

35 Y. Yang, H. Jia, S. Su, Y. Zhang, M. Zhao, J. Li, Q. Ruan and C. Zhang, A Pd-Based Plasmonic Photocatalyst for Nitrogen Fixation through an Antenna–Reactor Mechanism, *Chem. Sci.*, 2023, **14**(39), 10953–10961, DOI: 10.1039/D3SC02862C.

36 B. Roche, T. Vo and W.-S. Chang, Promoting Plasmonic Photocatalysis with Ligand-Induced Charge Separation under Interband Excitation, *Chem. Sci.*, 2023, **14**(32), 8598–8606, DOI: 10.1039/D3SC02167J.

37 Z. Li, C. Zhang, H. Sheng, J. Wang, Y. Zhu, L. Yu, J. Wang, Q. Peng and G. Lu, Molecular Cocatalyst of p -Mercaptophenylboronic Acid Boosts the Plasmon-Mediated Reduction of p -Nitrothiophenol, *ACS Appl. Mater. Interfaces*, 2022, **14**(33), 38302–38310, DOI: 10.1021/acsami.2c08327.

38 G. Joshi, K. Patrikar, U. Singhal, A. Mondal and S. Khatua, Controlling Plasmonic Charge Carrier Flow at a Nanoparticle–Molecule Interface Using Ligand Chemistry, *Nanoscale*, 2025, **17**(40), 23315–23322, DOI: 10.1039/D5NR02104A.

39 B. Nikoobakht and M. A. El-Sayed, Preparation and Growth Mechanism of Gold Nanorods (NRs) Using Seed-Mediated Growth Method, *Chem. Mater.*, 2003, **15**(10), 1957–1962, DOI: 10.1021/cm020732l.

40 A. Kar, M. Singh, D. Paital and S. Khatua, Establishing Surface Charge as a Key Control Parameter for Linker-Driven Tip-Specific Ordering of Anisotropic Gold Nanoparticles, *J. Phys. Chem. C*, 2021, **125**(43), 23895–23903, DOI: 10.1021/acs.jpcc.1c06550.

41 S. J. Patil and D. Kurouski, Tip-Enhanced Raman Imaging of Plasmon-Driven Dimerization of 4-Bromothiophenol on Nickel-Decorated Gold Nanoplate Bimetallic Nanostructures, *Chem. Commun.*, 2023, **59**(73), 10976–10979, DOI: 10.1039/D3CC02670A.

42 E. D. Emmons, J. A. Guicheteau, A. W. Fountain and A. Tripathi, Effect of Substituents on Surface Equilibria of Thiophenols and Isoquinolines on Gold Substrates Studied Using Surface-Enhanced Raman Spectroscopy, *Phys. Chem. Chem. Phys.*, 2020, **22**(28), 15953–15965, DOI: 10.1039/D0CP01125H.

43 S. Ghosh and L. Manna, The Many “Facets” of Halide Ions in the Chemistry of Colloidal Inorganic Nanocrystals,

Chem. Rev., 2018, **118**(16), 7804–7864, DOI: 10.1021/acs.chemrev.8b00158.

44 A. Dahi, A. Rogemont, Y. Brûlé, C. Labbez, R. Chassagnon, A. Coillet, E. Dujardin, J. Boudon and B. Cluzel, Gold Nanorod Growth and Etching Activated by Femtosecond Irradiation and Surface Plasmon Resonance, *J. Phys. Chem. C*, 2024, **128**(7), 3074–3081, DOI: 10.1021/acs.jpcc.3c08272.

45 K. G. Stamplecoskie and J. C. Scaiano, Light Emitting Diode Irradiation Can Control the Morphology and Optical Properties of Silver Nanoparticles, *J. Am. Chem. Soc.*, 2010, **132**(6), 1825–1827, DOI: 10.1021/ja910010b.

46 S. Roy, A. Rao, G. Devatha and P. P. Pillai, Revealing the Role of Electrostatics in Gold-Nanoparticle-Catalyzed Reduction of Charged Substrates, *ACS Catal.*, 2017, **7**(10), 7141–7145, DOI: 10.1021/acscatal.7b02292.

47 S. Khan, K. Patrikar, R. Sewak and A. Mondal, Correlating Ligand Properties with Photocatalytic Efficiency: A Computational Framework for Interface Engineering, *ACS Appl. Mater. Interfaces*, 2025, **17**(22), 32306–32315, DOI: 10.1021/acsami.5c03069.

48 L. Shi and A. Troisi, High-Throughput Screening of Molecule/Polymer Photocatalysts for the Hydrogen Evolution Reaction, *ACS Catal.*, 2025, **15**(9), 6690–6701, DOI: 10.1021/acscatal.5c01785.

49 M. Villa, A. Fermi, F. Calogero, X. Wu, A. Gualandi, P. G. Cozzi, A. Troisi, B. Ventura and P. Ceroni, Organic Super-Reducing Photocatalysts Generate Solvated Electrons via Two Consecutive Photon Induced Processes, *Chem. Sci.*, 2024, **15**(36), 14739–14745, DOI: 10.1039/D4SC04518A.

50 J. Khurgin, A. Y. Bykov and A. V. Zayats, Hot-Electron Dynamics in Plasmonic Nanostructures: Fundamentals, Applications and Overlooked Aspects, *eLight*, 2024, **4**(1), 15, DOI: 10.1186/s43593-024-00070-w.

51 H. Zhang and A. O. Govorov, Optical Generation of Hot Plasmonic Carriers in Metal Nanocrystals: The Effects of Shape and Field Enhancement, *J. Phys. Chem. C*, 2014, **118**(14), 7606–7614, DOI: 10.1021/jp500009k.

52 L. Khalil, S. Sabahat and W. Ahmed, Effect of Aspect Ratio on the Catalytic Activities of Gold Nanorods, *Catal. Lett.*, 2024, **154**(3), 1018–1025, DOI: 10.1007/s10562-023-04369-0.

53 Y. Pu and T. Pons, Gold Nanorod/Titanium Dioxide Hybrid Nanoparticles for Plasmon-Enhanced Near-Infrared Photoproduction of Hydroxyl Radicals and Photodynamic Therapy, *ACS Appl. Mater. Interfaces*, 2023, **15**(43), 49943–49952, DOI: 10.1021/acsami.3c05566.

54 G. T. Forcherio, D. R. Baker, J. Boltersdorf, A. C. Leff, J. P. McClure, K. N. Grew and C. A. Lundgren, Targeted Deposition of Platinum onto Gold Nanorods by Plasmonic Hot Electrons, *J. Phys. Chem. C*, 2018, **122**(50), 28901–28909, DOI: 10.1021/acs.jpcc.8b07868.

55 E. Cortés, W. Xie, J. Cambiasso, A. S. Jermyn, R. Sundararaman, P. Narang, S. Schlücker and S. A. Maier, Plasmonic Hot Electron Transport Drives Nano-Localized Chemistry, *Nat. Commun.*, 2017, **8**(1), 14880, DOI: 10.1038/ncomms14880.

56 A. Al-Zubeidi, Y. Wang, J. Lin, C. Flatebo, C. F. Landes, H. Ren and S. Link, D-Band, Holes React at the Tips of Gold Nanorods, *J. Phys. Chem. Lett.*, 2023, **14**(23), 5297–5304, DOI: 10.1021/acs.jpclett.3c00997.

57 P. Hohenberg and W. Kohn, Inhomogeneous Electron Gas, *Phys. Rev. [Sect.] B*, 1964, **136**(3), B864–B871, DOI: 10.1103/PhysRev.136.B864.

58 W. Kohn and L. J. Sham, Self-Consistent Equations Including Exchange and Correlation Effects, *Phys. Rev. [Sect.] A*, 1965, **140**(4), A1133–A1138, DOI: 10.1103/PhysRev.140.A1133.

59 Z. Futera and J. Blumberger, Electronic Couplings for Charge Transfer across Molecule/Metal and Molecule/Semiconductor Interfaces: Performance of the Projector Operator-Based Diabatization Approach, *J. Phys. Chem. C*, 2017, **121**(36), 19677–19689, DOI: 10.1021/acs.jpcc.7b06566.

60 J. Hutter, M. Iannuzzi, F. Schiffmann and J. VandeVondele, cp2k: Atomistic Simulations of Condensed Matter Systems, *Wiley Interdiscip. Rev.:Comput. Mol. Sci.*, 2014, **4**(1), 15–25, DOI: 10.1002/wcms.1159.

61 J. VandeVondele, M. Krack, F. Mohamed, M. Parrinello, T. Chassaing and J. Hutter, Quickstep: Fast and Accurate Density Functional Calculations Using a Mixed Gaussian and Plane Waves Approach, *Comput. Phys. Commun.*, 2005, **167**(2), 103–128, DOI: 10.1016/j.cpc.2004.12.014.

62 F. Weigend and R. Ahlrichs, Balanced Basis Sets of Split Valence, Triple Zeta Valence and Quadruple Zeta Valence Quality for H to Rn: Design and Assessment of Accuracy, *Phys. Chem. Chem. Phys.*, 2005, **7**(18), 3297, DOI: 10.1039/b508541a.

63 A. Schäfer, C. Huber and R. Ahlrichs, Fully Optimized Contracted Gaussian Basis Sets of Triple Zeta Valence Quality for Atoms Li to Kr, *J. Chem. Phys.*, 1994, **100**(8), 5829–5835, DOI: 10.1063/1.467146.

64 C. Hartwigsen, S. Goedecker and J. Hutter, Relativistic Separable Dual-Space Gaussian Pseudopotentials from H to Rn, *Phys. Rev. B: Condens. Matter Mater. Phys.*, 1998, **58**(7), 3641–3662, DOI: 10.1103/PhysRevB.58.3641.

65 S. Goedecker, M. Teter and J. Hutter, Separable Dual-Space Gaussian Pseudopotentials, *Phys. Rev. B: Condens. Matter Mater. Phys.*, 1996, **54**(3), 1703–1710, DOI: 10.1103/PhysRevB.54.1703.

66 N. S. Hush, Adiabatic Rate Processes at Electrodes. I, Energy-Charge Relationships, *J. Chem. Phys.*, 1958, **28**(5), 962–972, DOI: 10.1063/1.1744305.

67 R. A. Marcus, On the Theory of Electron-Transfer Reactions. VI. Unified Treatment for Homogeneous and Electrode Reactions, *J. Chem. Phys.*, 1965, **43**(2), 679–701, DOI: 10.1063/1.1696792.